



Lawrence Berkeley Laboratory
UNIVERSITY OF CALIFORNIA

EARTH SCIENCES DIVISION

Presented at the 1989 SPE Annual Technical Conference
and Exhibition, San Antonio, TX, October 8-11, 1989,
and submitted to *SPE Reservoir Engineering*

The Influence of Texture on Steady Foam Flow in Berea Sandstone

R.A. Ettinger and C.J. Radke

June 1989

For Reference

Not to be taken from this room



DISCLAIMER

This document was prepared as an account of work sponsored by the United States Government. While this document is believed to contain correct information, neither the United States Government nor any agency thereof, nor the Regents of the University of California, nor any of their employees, makes any warranty, express or implied, or assumes any legal responsibility for the accuracy, completeness, or usefulness of any information, apparatus, product, or process disclosed, or represents that its use would not infringe privately owned rights. Reference herein to any specific commercial product, process, or service by its trade name, trademark, manufacturer, or otherwise, does not necessarily constitute or imply its endorsement, recommendation, or favoring by the United States Government or any agency thereof, or the Regents of the University of California. The views and opinions of authors expressed herein do not necessarily state or reflect those of the United States Government or any agency thereof or the Regents of the University of California.

**The Influence of Texture on
Steady Foam Flow in Berea Sandstone**

R. A. Ettinger and C. J. Radke

Chemical Engineering Department
University of California

and

Earth Sciences Division
Lawrence Berkeley Laboratory
1 Cyclotron Road
Berkeley, California 94720

June 1989

This work was supported by the U.S. Department of Energy under Contract No. DE-AC03-76SF00098.

The Influence of Texture on Steady
Foam Flow in Berea Sandstone

R.A. Ettinger and C.J. Radke
Chemical Engineering Department
University of California
Berkeley, CA 94720

ABSTRACT

An understanding of texture, or bubble-size, evolution is paramount for modeling foam flow in porous media in that fine textures may impart large flow resistances. Bubble size, in turn, is determined by complicated lamellae creation and decay processes. We study, for the first time, the quantitative role of bubble size in the steady flow of strong foam through a $0.8\text{-}\mu\text{m}^2$ Berea sandstone. Inlet and outlet textures are determined from photomicrographs taken of bubbles flowing through specially designed visual cells. Concurrent measurements of pressure profiles and liquid saturation profiles by microwave attenuation are acquired for gas velocities ranging from 1 to 3 m/day and covering a foam quality range from 70 to 90%.

At steady state, liquid saturations remain constant near 35% independent of gas velocity. Moreover, measured foam-flow resistances practically do not vary with gas velocity over the studied range. Foam textures, however, do vary dramatically. For example, injected fine bubbles near $80\text{ }\mu\text{m}$ in diameter exit the sandstone with sizes around 300

μm . Powerful coalescence forces are the origin of this coarsening. Effluent bubble sizes increase slightly with increasing gas velocity, but are independent of the injected size.

A simple one-dimensional foam population-balance model is outlined to quantify the observed flow and texture behavior. At steady state, generation and coalescence mechanisms alter the foam texture over distances of less than about a centimeter. Agreement between the proposed model and the new bubble-size and flow data is adequate. The population-balance method proves to be a useful tool.

INTRODUCTION

Foam shows promise as a general fluid for improving mobility control in enhanced-oil-recovery processes. However, to optimize foam usage, knowledge of the rheological properties of foam in porous media is necessary. From the outset of foam studies in porous media [1], it was recognized that a very important factor controlling foam mobility is the bubble size distribution, or equivalently, the foam texture. In spite of this recognition, relatively little work has been directed towards measuring pertinent bubble sizes.

Marsden et al. [2] were apparently the first to attempt bubble-size measurements characteristic of flow through porous media. They obtained mean sizes for foam exiting sandpacks of unreported length for differing foam qualities and for differing surfactant types and concentrations. Their main finding was that bubble size, which was on the order of pore

bodies, correlated directly with foam mobility whereas quality did not. Surprisingly, they indicated that smaller bubbles compel a lower flow resistance in porous media. This finding is at odds with more recent work which argues for a decreasing mobility with a decreasing bubble size [3-9].

More recently, Treinen, Brigham, and Castanier [10] also examined foam bubbles exiting sandpacks for differing surfactant concentrations, but at flow velocities close to one meter per day. These researchers found that bubble sizes observed in visual cells were a factor of 10 larger than typical pore sizes in the sandpacks. Hence, they were hesitant to correlate their flow results with texture.

Friedmann and Jensen [11] observed the bubble texture exiting several different porous media including steel-wool packs, sandpacks, and Berea sandstone. They utilized short cores and rather high velocities up to several hundred meters per day. Generally, at constant quality, increasing velocities decreased the bubble size. No concomitant pressure-drop data were given.

Thus, to date, the few studies on bubble texture related to flow mobility in porous media have been mainly qualitative. No effort was directed towards modeling flow with the measured textures. This work attempts, as far as possible, quantitative evaluation of bubble texture and its relationship to foam-flow behavior. Using carefully designed visual cells, we pursue steady inlet and outlet bubbles sizes for a 0.8-

μm^2 Berea sandstone. At constant liquid velocity, total flow rates are varied from 0.9 to 2.4 m/day covering a quality range from 70 to 90%. Simultaneous steady pressure profiles and liquid saturation profiles from scanning microwave attenuation are also determined. With the foam-texture measurements in hand, a simple population-balance model of foam flow is proposed and compared to the new experimental flow rate-pressure drop results.

We begin with a brief description of our experimental procedures and results. Basically, the recent findings of Persoff et al. [9] and De Vries and Wit [12] are reconfirmed in that liquid saturations for steady-state foam flow are constant at a few units above connate saturation and are independent of gas flow rates. Also, the pressure-drop behavior of foam at constant liquid velocity is found to be practically independent of gas velocity, again in agreement with Persoff et al. [9]. Moreover, the sandstone porous medium rapidly coarsens injected small bubbles to an average size of about 1.5 pore-body diameters. This same effluent bubble size appears for foam produced in-situ. Following the results section, we present a population-balance model for foam transport. The theory considers only the mean bubble size [13] and incorporates simplified, semi-empirical expressions for the rates of bubble generation and decay. Comparison of theory and experiment follows. Adequate agreement is seen. Another major finding of this section is that, in contrast to other studies [5-7], bubble coalescence plays a major role in determining in-situ foam texture. Conclusions complete the paper.

EXPERIMENT

Apparatus

A schematic of the foam-flow apparatus is shown in Fig. 1. The porous medium is a fired Berea sandstone 20 cm (8 in.) long x 10 cm (4.0 in.) wide x 1.2 cm (0.4 in.) deep. Distribution channels are machined into the ends of the sandstone to induce uniform axial flow. The sandstone has an absolute permeability of $0.8 \mu\text{m}^2$ and a porosity of 0.24. To permit liquid saturation measurements by microwave attenuation, the Berea slab is both thin and is epoxied into a core holder constructed of 0.64-cm thick polystyrene, a material that is nearly transparent to microwaves. Unfortunately, the fragile core holder hindered measurements at high velocities, where large foam pressure gradients emerge, and also prevented application of a back pressure. Pressure taps are machined into the core along one side. During many experiments foam was pregenerated in a 5.1 cm (2 in.) long, 2.5 x 2.5 cm (1 x 1 in.) wide, $0.5\text{-}\mu\text{m}^2$ unfired Berea core. Foam texture is observed in visual cells (to be described) placed just before and after the $0.8\text{-}\mu\text{m}^2$ Berea core.

Pressure profiles are measured with four differential transducers (Validyne, Model DP-15) with 690, 520, 340, and 140 kPa (100, 75, 50, and 20 psi) diaphragms and located respectively, slightly upstream, 5.1, 10, and 15 cm (0, 2, 4, and 6 in.) from the core inlet. The working side of each transducer is connected to the core through flexible Teflon tubing filled with the surfactant solution while the null side is open to the atmosphere. At steady state, gas is observed just at the inlet of the Teflon tubing, indicating that the gas-phase pressure is detected.

Signals from the transducers are sent to a 10 channel demodulator (Validyne, Model MC1) and the voltages are recorded continuously (Linear, Model 585).

Foamer solution is delivered with either a liquid chromatography pump (Altex, Model 100A) or a high pressure piston pump (ISCO, Model #314). The nitrogen flow rate is controlled with a mass flow controller (Brooks, Model #5850).

The surfactant solution is a degassed, saline solution containing 0.83 wt% NaCl (Mallinckrodt, reagent grade) with 0.83 wt% active C_{14-16} α -olefin sulfonate surfactant (Bioterg AS-40, Stepan). The surface tension, measured by the Wilhelmy-plate method, is 33 mN/m, and the solution viscosity is 1.0 mPa·s at ambient temperature.

Liquid saturation profiles are measured by scanning microwave attenuation which, after calibration, detects the water content in the core by the Beer-Lambert absorption law [14]. Our microwave source is a mechanically tuned Gunn-Oscillator (Alpha Industries, Model CMF624), adjusted to emit microwaves with a frequency of 21.3 GHz (i.e., a wavelength of 1.4 cm) and a maximum power of 215 mW. The waves are collimated by a Fresnel lens to a 1 cm^2 nominal beam size. Both incident and transmitted power are measured by waveguide detectors (Wavetek - Pacific Instrument Inc., Model #15271) and a RF Power Meter (Wavetek - Pacific Instrument Inc., Model #1045/01). Scanning of the sandstone is accomplished with a Slo-Syn stepper motor (The Superior Electric Company,

Model M111-FD12) and motor driver (Anaheim Automation, Model DPF-37). An IBM PC-XT is used for control and data acquisition, taking 30 saturation measurements at 0.51 cm (0.2 in.) intervals. Due to the metal fittings at each end of the core, saturation data near the entrance and exit are precluded. Considerably more information on the scanning microwave attenuator is available elsewhere [15,16].

In spite of the long wavelength of the microwaves, we were initially concerned that the finely dispersed foam bubbles inside the core might interfere with the water-saturation measurements. To allay this concern the attenuation was determined for a surfactant solution and a bulk, foamed surfactant solution containing the same amount of water. Measured attenuation was identical for several different surfactant solutions and for several different foam textures, giving us confidence in the microwave technique [16,17].

To ascertain the foam bubble-size distributions, in-line viewing cells were constructed. These have the distinctive feature of allowing examination of a single layer of bubbles. Each viewing cell consists of a cylindrical piece of plexiglass with a thin disc of uniform thickness machined into one side. This side is then attached to a second, smooth cylindrical piece of plexiglass, and inlet and exit lines are drilled into the machined-out disc. It is crucial that the viewing area have a gap thickness that is less than the average bubble diameter. The foam bubbles are then deformed from their natural three-dimensional polyhedral shape into two-dimensional shapes that permit clear focusing under 20X

magnification with a 35 mm camera (Nikon Nikkormat) and attached bellows (Nikon, PB-4) and 50-mm lens (Nikkor). To measure a range of bubble sizes, two separate viewing cells with different machined gap depths were constructed. The first cell, with a viewing region 0.25 mm (0.01 in.) deep and 3.1 cm (1.2 in.) in diameter, is used for the larger bubbles with diameters near 300 μm . The second cell, which has a viewing region 0.051 mm (0.002 in.) deep and 7.0 cm (2.8 in.) in diameter, is used to measure bubbles with diameters around 100 μm . Several photomicrographs of the foam flowing through the viewing cell are taken and enlargements are made such that the bubble diameters range in absolute size from 1 to 25 mm. Number size distributions are determined by manual counting from the enlarged photographs using a particle-size counter (Zeiss, Model TGZ-3). The size distribution is initially obtained in terms of the diameters of the two-dimensional bubbles. It is then converted to the diameters of equivalent undeformed spheres. For a reliable size distribution, at least 400 bubbles should be counted [18]. Note that the volume of the average undeformed sphere is simply the inverse of the average bubble density, n_F , used later in the population-balance model.

Foam bubbles can be produced at the exit face of a porous medium without much foam actually being present inside the medium [19]. Accordingly, bubble sizes measured in external visual cells may not be representative of in-situ texture. To address this issue, with the pregenerating core in-line, we lowered the flow velocity below the critical velocity for bubble generation by snap off and/or division [7,19]. At an outlet velocity of 0.91 m/day (3.0 ft/day) and at an outlet

gas fractional flow of 0.9, the open circles in Fig. 2 indicate a low pressure drop across the 20-cm working core of about 36 kPa (5.3 psi). Only a weak foam persists in the medium, but, nevertheless, gas bubbles are seen in the downstream viewing cell, as illustrated in Fig. 3a. These bubbles are quite large, near 700 μm . Such coarse foam is, in our opinion, characteristic of bubbles generated solely at the core exit face.

When the total outlet velocity, again at a gas fractional flow of 90%, is raised to 2.5 m/day (8.1 ft/day), a fine textured foam appears in the viewing cell, as seen in Fig. 3b. Here, the bubble sizes are near 300 μm . That this foam is characteristic of in-depth bubbles is noted by the closed circles in Fig. 2, which indicate an increase in pressure drop by a factor of about 10 to about 1.7 MPa/m (74 psi/ft). A strong foam has now been produced within the core. Since the mean pore-body sizes of similar Berea sandstones are near 200 μm [20], our observed bubble sizes seem to be reasonable estimates of in-situ sizes, especially when compared to those seen in companion micromodel studies [21,22].

A second concern about bubble-size validity is possible coalescence in the lines leading to and from the viewing cells. Happily, lengthening the line from the Berea slab to the exit viewing cell from 5.1 cm (2 in.) to 38 cm (15 in.) caused no measurable change in the bubble-size distribution. Other factors that might vitiate the size measurements are variations of foam texture in time and in position through the viewing cell. Although our tests were not extensive, we found no important differences due to these two factors. Of course, it is not possible to

eliminate conclusively all core inlet and exit artifacts. Nevertheless, our bubble-size measurements appear to be diagnostic of those occurring inside the porous medium.

A point of emphasis arising from Fig. 2 is that our critical velocity for strong foam formation [19] is quite low, near 1 m/day, in agreement with the work of Persoff et al. [9]. Conversely, velocities measured by Friedmann, Chen, and Gauglitz, also for Berea sandstone, fall in a much higher range of several tens of m/day [7]. All the flow studies reported in this paper are above the critical velocity for generation of a so-called strong foam [19].

Procedures

The core is vacuum saturated and replenished with approximately 5 PV of surfactant solution. Nitrogen and foamer solution are then injected either directly into the core or first into the pregenerating core until steady state is achieved. If the pregenerating core is on-line, a steady-state foam texture is first produced with flow directed to the atmosphere. This foam is then directed into the surfactant-filled downstream core. Steady state in the working core is typically established after about 10 PV and is assessed both by unchanging pressure and liquid saturation profiles and by observing constant inlet and effluent foam textures. Once the steady state is reached, photomicrographs are taken of the foam texture in each viewing cell. The gas flow rate is then varied to reach new steady states. For all flow experiments, the liquid flow rate was kept constant at a value of 0.27 m/day (0.9 ft/day). Additional details

on the experimental apparatus and procedures are available in the thesis of Ettinger [16].

RESULTS

Closed circles in Fig. 2 reflect a typical pressure profile for a pregenerated foam flow experiment at the listed exit conditions. Again, the large average pressure gradient of 1.7 MPa/m (74 psi/ft) is indicative of strong foam formation. With such large pressure gradients and an atmospheric exit pressure, gas compressibility cannot be ignored. For example, for the particular flow experiment in Fig. 2, the inlet total velocity is 0.79 m/day (2.6 ft/day) and the inlet gas fractional flow is 0.65. Thus, in a single flow experiment, the gas velocity increases down the core by a factor of 3 and the foam quality (i.e., gas fractional flow) increases by 40%. In the figures to follow, we report all flow conditions relative to the core exit, or equivalently, relative to one atmosphere of pressure.

It is noteworthy in the strong foam pressure profile of Fig. 2 that the quadratic-pressure behavior typical of a compressible gas is not apparent. We argue later that this is due to local bubble texture alteration. Inlet bubbles sizes for the strong foam in Fig. 2 are near 80 μm while those exiting are near 300 μm (cf. Fig. 3b). Nevertheless, the profile does not exhibit significantly larger pressure gradients near the core inlet. Likewise for in-situ generated foam (i.e., no injected bubbles), we find that the pressure gradients near the core inlet are not significantly smaller than those downstream. Apparently, the porous

medium shapes the foam texture very close to the inlet face. The pressure profile data of Persoff et al. [9] and De Vries and Wit [12] also support this observation while those of Friedmann, Chen, and Gauglitz [7] at much higher velocities indicate significant texture alterations occurring over several inches of distance.

Figure 4 summarizes the effect of velocity on the strong foam pressure drop across the core per unit length at fixed liquid velocity. Closed symbols correspond to the 80- μm pregenerated foam while open symbols reflect foam generated in-situ. Pregenerated foam pressure drops are consistently higher than those of the in-situ generated foam due to the initial fine texture. Repeat experiments do show some scatter. The most likely origin of this scatter is variations in the liquid flow rates caused by operating the liquid chromatography pump near its lower limit of capacity.

Steady pressure drops for foam flow in Fig. 4 are practically independent of gas flow rate, although there is a slight increasing trend with increasing gas velocity. The identical observation was made recently by Persoff et al. [9].

Figure 5 displays the companion, steady-state water saturation profiles for the various gas flow rates. Liquid saturations are consistently between 30 and 40%, essentially independent of gas velocity. Observe that S_w is constant with only a slight decrease along the core even though the gas velocity increases with axial position due to

compressibility. Constant liquid saturations independent of flow velocity are also in exact agreement with the findings of Persoff et al. [9] and with those of De Vries and Wit [12].

Figure 6 shows both a measured injected and effluent bubble-size distribution for an outlet total velocity of 0.91 m/day (3.0 ft/day) and a outlet gas fractional flow of 0.70. Gas compressibility is the reason why the inlet velocity and gas fractional flow are smaller than those at the exit. As noted above, the pregenerated foam has an average bubble diameter of approximately 80 μm , corresponding to a bubble density of $n_F = 3900 \text{ mm}^{-3}$, while the average exiting bubble diameter and bubble density are 290 μm and 78 mm^{-3} , respectively. As expected, the larger bubbles exhibit a larger spread in sizes. Expansion of the 80- μm bubbles from a pressure of 420 kPa (61 psi) to atmospheric pressure is insufficient to explain this almost two-order magnitude drop in bubble density.

Figure 7 compares the measured effluent bubble density for the pregenerated foam in Fig. 6 with one that is generated in-situ, with both experiments run under the same flow conditions. These two bubble-size distributions are essentially replicates. Hence, the porous medium shapes the foam to its liking no matter what type of foam is supplied. The constancy of exit bubble size independent of inlet size suggests that the drastic decline in bubble texture seen in Fig. 6 is not due primarily to breakage at the core face. Also, our pressure profiles indicate that generation and coalescence mechanisms shape the foam over very short distances near the core inlet.

A summary of the measured effluent mean bubble densities, n_{FL} , and sizes, D_{BL} , is graphed as a function of total velocity in Fig. 8. Because bubble density varies inversely with the cube of the measured mean bubble size, it is difficult to obtain precise estimates of n_F . Nevertheless, as the gas velocity is increased the exit bubbles definitively become somewhat larger. Typically, one anticipates that higher velocities lead to finer textured foams [11]. Figure 8 shows just the opposite. In Fig. 8, however, only the gas velocity is increased, not the liquid velocity. Our proposed explanation for the bubble-size decline, as outlined in the theory section below, is that higher gas velocities increase the rate of bubble coalescence and accordingly, coarsen the foam. Choice of the solid line in Fig. 8 is explained below.

THEORY

Background

Even in an oil-free porous medium, foam consists of at least three flow regions. It must not be viewed as a single-phase fluid. For water-wet media, the aqueous surfactant solution flows in the smaller pore channels as dictated by the liquid saturation and the corresponding capillary pressure. Liquid flow then obeys Darcy's multiphase law according to the standard, wetting-phase relative permeability and evaluated at the liquid saturation in the medium [9,23,24]. Very little liquid transports in the form of flowing lamellae or through networks of stagnant lamellae. In-situ foam quality is, therefore, much higher than that injected.

Foam is the nonwetting phase and occupies the larger pores in the medium. A major portion of the foam bubbles is trapped as trains in the intermediate-sized pores. Tracer [7,23,25] and micromodel visual [21] studies suggest that between 30 and 90% of the gas-occupied pore space is stagnant. Recently Friedmann, Chen, and Gauglitz detected trapped gas saturations in Berea sandstone near 80% [7]. More importantly, they observed that the amount of stagnant foam was reasonably independent flow rate even at high rates near 30 m/day (100 ft/day). Since our velocities are much lower and also our velocity range is rather narrow, we take the trapped gas to be a constant in the modeling effort. Of course, high enough pressure gradients [8] should mobilize some of the stagnant foam.

In the remaining largest pores which form the least resistant connected flow paths, foam parades as a bubble caravan. The high foam pressure gradients and the lack of sensitivity to gas flow rates, which we and others [9,12] observe, argue against much, if any, free gas present in the medium. Because the mobile foam resides in the very largest pores, we write a modified form of Darcy's law:

$$U_g = - \frac{k k_{rgF}}{\mu_e} \nabla P_g \quad , \quad (1)$$

where U_g is the flowing foam superficial velocity, P_g is the gas pressure, k is the absolute permeability, k_{rgF} is the relative permeability, and μ_e is the effective or apparent viscosity. k_{rgF} is the usual relative permeability of the nonwetting phase but evaluated at the flowing gas saturation, S_F . Since S_F may be small due to the possibly

large amount of trapped gas, k_{rgF} may also be quite small. For example, a 35% liquid saturation (cf. Fig. 5) and a 15% flowing gas fraction [7] sets S_F at about 10%. This in turn predicts that $k_{rgF} \sim 0.1$, using known relative permeability curves of Berea sandstone [7,26]. In our modeling effort the exact value of k_{rgF} need not be specified.

Equation (1) is useful only in so far as μ_e is a known function. The most important property of μ_e is that it increases with increasing texture so that smaller bubbles produce larger flow resistances. Both experimental and theoretical evidence to date suggest the following form for μ_e [3,4,7]:

$$(\mu_e - \mu_g)/\mu = A n_F D_b^3 (\sigma/\mu U_g)^{1/3}, \quad (2)$$

where μ is the liquid viscosity, μ_g is the gas viscosity, D_b is a characteristic pore-body diameter, taken here as 200 μm [20], σ is the equilibrium surface tension, n_F is the local bubble density, and A is a scaling coefficient. For fixed liquid and flowing gas saturations and for a fixed surfactant type and concentration, A is a constant [3,4].

Equation (2) teaches that the viscous resistance of flowing foam is linearly proportional to bubble density, ostensibly because most of the hydrodynamic resistance of the bubbles is localized near the lamellae [3,4]. It also teaches that flowing foam is shear thinning. Implicit in Eqn. (2) is the restriction that the local pressure gradients exceed the mobilization gradient [8]. Typical values for μ_e in this work (cf. Fig. 4) and in that of Persoff et al. (see Figs. 10 and 11 of [9]) range

approximately from 10 to 100 mPa·s. Flowing foam can exhibit effective flow resistances in porous media that are several orders of magnitude larger than that of water.

Even though the percolating bubble trains fill only a relatively small percentage of the pore space, the flowing region is paramount to the lamellae "making" and "breaking" processes [24] that evolve foam texture. Bubbles are generated by sporadic gas invasion into and snap-off in germination sites [19,27,28]: that is, intermittently, liquid-filled pore throats connected to pore bodies that have sufficiently large body to throat aspect ratios and that are accessible to the backbone channels supporting foam flow [29]. Bubble or lamella division at branch points can also play a major role in generating fine bubbles [29,30]. In oil-free porous media foam lamellae break primarily by flowing through pore bodies or junctions, called termination sites, where they are stretched thin enough to be unstable to infinitesimal disturbances [22,29]. High capillary pressures thin the lamellae by suction at the Plateau borders. Hence, flowing lamellae are very vulnerable to breakage at low wetting liquid saturations. For the 30 to 40% water saturations we measure, capillary pressures are large and considerable lamellae breakage occurs. This explains why the bubble density declines so drastically in Fig. 6. In fact, we argue that except very close to the core inlet, the rates of bubble coalescence and generation are almost equal in our experiments. After Khatib, Hirasaki, and Falls [31], we designate this flow state as the coalescence regime.

The experiments of Persoff et al. with incompressible foam [9] are also in this coalescence regime. Consequently, their bubble density should have remained constant along the core, except again in a very small region near the inlet face where a net generation takes place. Accordingly, Eqns. (1) and (2), along with the experimental observation that at steady state the foam-flow resistance is directly proportional to V_l/V_g (see Fig. 12 of [9]), suggest the following velocity dependencies for the flowing bubble concentration:

$$n_F \sim V_l/V_g^{2/3} \quad (3)$$

Equation (3) may be rationalized by arguing that increased liquid flow generates more bubbles while increased gas flow coarsens the foam through increased lamellae breakage. We will use Eqn. (3) as a guide for setting some of the parameters in our population-balance model described below.

Model

As above, let $n_F(x)$ denote the mean bubble density, or the number of bubbles per available flowing volume, as a function of axial position, x , along the linear core. A steady-state population balance on the average flowing bubble size then reads [5,7,13]:

$$\frac{d(n_F U_g)}{dx} = r_g - r_c - r_t, \quad (4)$$

where r_g , r_c , and r_t are the rates of bubble generation, coalescence, and trapping, respectively, per unit bed volume. As discussed in the previous section, the trapped gas saturation remains constant over the range of

velocities studies here. Therefore, the net trapping rate is set to zero.

For constant surfactant concentrations, constant gas and liquid saturations, and at a fixed liquid velocity, we write the coalescence rate as:

$$r_c = k_{-1} U_g^n n_F, \quad (5)$$

where k_{-1} is a coalescence rate constant. Equation (5) is motivated by the idea that foam lamellae disappear in proportion to their flux into termination sites, $n_F U_g$. In addition, higher gas velocities lead to a higher probability of breakage because the stretched, vulnerable lamellae do not have sufficient time for healing from the surrounding foamer solution [22]. Stated in other words, the limiting capillary pressure for the onset of coalescence is a function of gas velocity [31]. Hence, the power index n in Eqn. (5) should be somewhat larger than but close to unity. The coalescence rate constant depends strongly on the surfactant type and concentration with weak surfactants and low concentrations making k_{-1} quite large, possibly large enough to prevent any steady foam in the medium. Also, k_{-1} depends strongly on the liquid saturation. For robust surfactants it will be small at high liquid saturations and then rise steeply as the saturation falls to a value approaching the limiting capillary pressure [22,31].

The foam generation rate by snap-off should be independent of texture as long as the bubble size does not fall to quite a low value [7]. For constant liquid velocity and saturation we write simply that

$$r_g = k_1 U_g^m, \quad (6)$$

where k_1 is a generation rate constant and the power index m should not be large. k_1 varies with liquid saturation, but probably not as strongly as does k_{-1} . The generation rate constant should not depend on the surfactant formulation [27,28]. Equation (6) is valid only when the critical velocity or pressure gradient necessary to initiate snap-off is exceeded [7,19], otherwise $k_1 \equiv 0$ [7].

Lamellae division is another mechanism to enhance the texture. The rate of bubble division is, to a first approximation, proportional to the flux into division sites. Thus, when n is close to unity in Eqn. (5), bubble-division rates are difficult to specify separately from a net lower coalescence rate. We do not attempt this separation.

In addition to describing bubble-density evolution by Eqn. (3), a statement is required about overall mass conservation of the gas phase. For an ideal gas this statement reduces to

$$P_g U_g = P_{gL} U_{gL}, \quad (7)$$

where P_{gL} and U_{gL} are the gas pressure and gas velocity, respectively, at the core exit.

Equations (1) - (7) reduce to two, first-order, coupled ordinary differential equations describing the pressure and bubble concentration profiles. They are solved numerically subject to a fixed inlet texture

and a known outlet pressure [16]. These conditions correspond to our experimental procedures.

Solid lines in Figs. 9 and 10 report dimensionless bubble density and foam pressure profiles from the simple, steady population-balance model. Two nondimensional parameters appear:

$$Da \equiv k_{-1} U_{gL}^{n-1} L, \quad (8)$$

and

$$\kappa \equiv \mu_{eL} U_{gL} L / k_{rgF} P_{gL}, \quad (9)$$

where μ_{eL} denotes the effective foam viscosity in Eqn. (2) but evaluated at the column exit. κ reflects a characteristic difference in pressure across the core compared to the absolute exit pressure. Hence, it gauges the importance of compressibility. Da is a Damköhler number that assesses the ratio the column length, L , to a characteristic distance for coalescence, U_{gL}^{1-n}/k_{-1} . In Figs. 9 and 10, $m < n$ so that increasing gas velocities lead to net foam coarsening. Also, the inlet bubble density is zero, so the foam is generated in-situ within the porous medium rather than injected externally. Because of compressibility, the gas velocity increases along the column. All curves are compared at equal outlet pressures and velocities.

As κ increases in Fig. 9, more effect of compressibility is evident. Straight lines drawn conceptually through the origin and with the initial slope of the solid curves correspond to the bubble concentration rise due

to generation only. Higher κ values generate fine foam more quickly because of the comparatively lower gas velocities at the core inlet. For the chosen Damköhler number of 10, the influence of coalescence is seen near $x/L = 0.2$ where the bubble density no longer continues to rise. When $\kappa \leq 0.1$ the foam is practically incompressible, and a constant bubble size emerges where the rates of coalescence generation and coalescence are identical. From Eqns. (5) and (6) and a net zero rate, $r_g - r_c = 0$, the resulting equilibrium bubble density is given by

$$n_{F\infty} = k_1/k_{-1} U_g^{n-m} . \quad (10)$$

Bubble sizes are finer in Fig. 9 with compressible foam, $\kappa > 0.1$, because gas velocities are lower throughout the core causing less coalescence. All textures eventually coarsen to unity since the exit gas velocity is fixed.

The companion pressure profiles in Fig. 10 show higher pressure drops at higher κ values reflecting the finer textures seen in Fig. 9. In the net generation region of the core for $x/L \leq 0.2$ all curves exhibit smaller pressure gradients. Thereafter, the profiles are almost linear, rather than parabolic as in compressible flow of Newtonian fluids. Coarsening of the foam texture along the core is the explanation.

When the coalescence rate constant is large such that $Da \geq 50$, then the rates of bubble creation and decay are almost in balance throughout the porous medium. Hence, Eqn. (10) is obeyed except at the core face. Dashed lines in Figs. 9 and 10 display this local equilibrium state. Even

for $Da = 10$, the local-equilibrium approximation proves acceptable. Equation (10) reveals that it is the ratio of the generation and coalescence rate constants that determines the mean bubble size that evolves in the porous medium.

COMPARISON OF THEORY AND EXPERIMENT

Five unknown parameters arise in the theory: k_1 , k_{-1} , m , n , and $\eta \equiv A/k_{rgF}$. Fortunately, we are not at liberty to adjust them over wide ranges. As enunciated earlier, our experimental observations and those of others at comparable velocities [9,12] indicate that local equilibrium is a good approximation. That is, at steady state most of the texture adjustment is focused in a small region very close to the core inlet. Hence, Eqn. (10) adequately describes the texture profile. Comparison of Eqn. (10) with the experimental observations embodied in Eqn. (3) reveals that $n - m = 2/3$. Since n is expected to be near unity, we set $n = 1$ and $m = 1/3$ as listed in Table 1. Use of Eqn. (10) and the measured outlet textures in Fig. 8 then permit calculation of k_1/k_{-1} . The solid line in Fig. 8 corresponds to a best fit and yields a value of k_1/k_{-1} of $7.84 \text{ (cm/s)}^{2/3} \text{ mm}^{-3}$. Remember in Fig. 8 that small differences in measured bubble sizes can lead to major changes in bubble density. Hence, although the bubble density clearly falls with increasing gas velocity, the $-2/3$ exponent is not unambiguous.

Next k_{-1} is set, somewhat arbitrarily, so that most all of the texture adjustment is accomplished within a centimeter from the core face. The resulting magnitudes of k_1 and k_{-1} are displayed in Table 1.

Finally, the flow-resistance parameter, $\eta \equiv A/k_{rgF}$, is adjusted to give reasonable representation of our entire set of pressure profiles. Table 1 indicates that $\eta = 1.3$. This value is of the same order of magnitude as that found by Friedmann, Chen, and Gauglitz [7] and is consistent with preliminary, a priori estimates [4]. Pressure profiles are relatively sensitive to the value chosen for η .

Figures 11 and 12 compare typical measured and theoretical bubble density and pressure profiles both for pregenerated (closed symbols) and in-situ (open symbols) produced strong foam. Additional profile data are available elsewhere [16]. Solid lines follow the population-balance model while dashed lines obey the local-equilibrium approximation. Generally, measured and predicted textures are always in good agreement. Predicted pressure profiles, however, tend to over estimate the in-situ generated foam behavior and to under estimate the pregenerated foam behavior. In particular, the predicted sharp rise in pressure near the inlet upon injection of a fine textured foam is never seen experimentally. Possibly some foam collapse may take place in the inlet distribution channels as the pregenerated bubbles attempt to enter the sandstone medium. It is also true that small errors in measuring these fine bubble sizes results in rather large changes in n_F . Nevertheless, Fig. 4 does confirm that pressure drops for the pregenerated foam are generally higher than those for the in-situ generated foam. In view of the scatter typically seen in repeated foam flow experiments (cf. the various solid symbols in Figs. 11 and 12), we consider the model predictions to be adequate, but not

sterling. Since the measured textures and predicted foam-flow behavior are consistent, we assert that the population-balance approach has merit.

It is clear that a wider range of gas flow rates needs to be investigated to build confidence in the trend reported in Fig. 8 of a coarser foam at higher gas velocity. In addition, the role of liquid velocity needs to be studied. Equation (3) demands a finer textured foam at higher liquid velocities. Unfortunately, we have not studied the role of liquid velocity on texture. Clearly, in foam-flow experiments, it is not wise to vary only fractional flow. Effects of gas and liquid velocity need to be considered individually [9].

We caution that the approximation of local-equilibrium textures is not expected to hold except in the coalescence flow regime. This regime in turn holds when the liquid saturation is low enough and the corresponding capillary pressure is high enough so that coalescence rates can come into balance with generation rates. During transient displacement coalescence should be minimal when liquid saturations are high. Here, texture alteration should be dominated by generation rates only. Transient displacement with foam likely does not proceed through a sequence of local steady states as in Buckley-Leverett theory.

CONCLUSIONS

We list the following main points for steady foam flow in a $0.8\text{-}\mu\text{m}^2$ Berea sandstone:

1. Liquid saturations are constant at several units above connate saturation and are independent of gas flow rate. Likewise, foam pressure gradients are also sensibly independent of gas flow rate when the liquid velocity is fixed. Both of these observations strikingly confirm recent independent work from our laboratory [9].
2. Either injection of a fine texture foam, with bubble sizes near $80\text{ }\mu\text{m}$ or injection of unfoamed gas and surfactant solution yields effluent bubble sizes near $300\text{ }\mu\text{m}$. The porous medium shapes the foam to its own liking through strong making and breaking processes.
3. Except very close to the inlet face of a linear core, coalescence and generation rates are almost in balance. We designate this flow state as the coalescence regime.
4. A proposed population-balance model for foam flow represents our new bubble-size and pressure-profile data adequately. The main premise of the model is that finer textured foam leads to larger flow resistance. The population-balance approach for modeling foam-flow behavior appears to be both valid and useful.

NOMENCLATURE

- A = effective viscosity scaling coefficient (dimensionless)
 D_b = average pore-body diameter (m)
 D_B = average bubble diameter (m)
 D_{BL} = average bubble diameter at core exit (m)

- $Da = k_{-1} U_{gL}^{n-1} L$, Damköhler number (dimensionless)
 f_g = gas fractional flow (dimensionless)
 k = absolute permeability (m^2)
 k_{rgF} = relative permeability to flowing foam (dimensionless)
 k_1 = generation rate constant ($(cm/s)^{2/3} mm^{-3}$)
 k_{-1} = coalescence rate constant (m^{-1})
 L = core length (m)
 m = generation rate gas-velocity order (dimensionless)
 n = coalescence rate gas-velocity order (dimensionless)
 n_F = local bubble density (m^{-3})
 n_{FL} = exit bubble density (m^{-3})
 $n_{F\infty}$ = equilibrium bubble density (m^{-3})
 P_g = gas-phase pressure (Pa)
 P_{gL} = exit gas-phase pressure (Pa)
 r_c = rate of coalescence ($m^{-3} s^{-1}$)
 r_g = rate of generation ($m^{-3} s^{-1}$)
 r_t = rate of trapping ($m^{-3} s^{-1}$)
 S_F = flowing foam saturation (dimensionless)
 S_w = liquid saturation (dimensionless)
 U = total superficial velocity (m/day)
 U_g = gas superficial velocity (m/day)
 U_{gL} = gas exit superficial velocity (m/day)
 U_l = liquid superficial velocity (m/day)
 x = axial distance along core (m)

Greek

- η = A/k_{rgF} , foam-flow resistance factor (dimensionless)
 κ = $\mu_{eL} U_{gL} L/k_{rgF} P_{gL}$, compressibility factor (dimensionless)
 μ = liquid viscosity (Pa.s)
 μ_e = effective foam viscosity (Pa.s)
 μ_{eL} = effective foam exit viscosity (Pa.s)
 μ_g = gas viscosity (Pa.s)
 σ = equilibrium surface tension (N/m)

ACKNOWLEDGMENTS

This work was supported by the U.S. Department of Energy, under Contract No. DE-AC03-76SF00098 to the Lawrence Berkeley Laboratory of the University of California.

REFERENCES

1. Fried, A.N.: "The Foam Drive Process for Increasing the Recovery of Oil," Report of Investigation 5866, U.S. Bureau of Mines (1961).
2. Marsden, S.S., Eerligh, J.J.P., Albrecht, R.A., and David, A.: "Use of Foam in Petroleum Operations," 7th World Petroleum Congress, Mexico City (April 1967) 235-242.
3. Hirasaki, G.J and Lawson, J.B.: "Mechanism of Foam Flow in Porous Media: Apparent Viscosity in Smooth Capillaries," SPEJ (April 1985) 176-190.
4. Ginley, G.M. and Radke, C.J.: "The Influence of Soluble Surfactants on the Flow of Long Bubbles Through a Cylindrical Capillary," presented at the Symposium on Advances in Oil Field Chemistry, Third Chemical Congress of the North American Continent and 195th National Meeting of ACS, Toronto, Canada, June 5-11 (1988).
5. Falls, A.H., Hirasaki, G.J., Patzek, T.W., Gauglitz, P.A., Miller, D.D., and Ratulowski, T.: "Development of a Mechanistic Foam Simulator: The Population Balance and Generation by Snap-Off," SPERE (August 1988) 844-892.
6. Falls, A.H., Musters, J.J., and Ratulowski, J.: "The Apparent Viscosity of Foams in Homogeneous Beadpacks," SPERE (May 1989) 155-164.

7. Friedmann, F., Chen, W.H., and Gauglitz, P.A.: "Experimental and Simulation Study of High-Temperature Foam Displacement in Porous Media," SPE/DOE 17357, presented at the 1988 SPE/DOE Enhanced Oil Recovery Symposium, Tulsa, OK, April 17-20.
8. Rossen, W.R.: "Theories of Foam Mobilization Pressure Gradient," SPE/DOE 17358, presented at the 1988 SPE/DOE Enhanced Oil Recovery Symposium, Tulsa, OK, April 17-20.
9. Persoff, P., Radke, C.J., Pruess, K., Benson, S.M. and Witherspoon, P.A.: "A Laboratory Investigation of Foam Flow in Sandstone at Elevated Pressure," SPE 18781, presented at the 1989 SPE California Regional Meeting, Bakersfield, CA, April 5-7.
10. Treinen, R.J., Brigham, W.E., and Castanier, L.M.: "Apparent Viscosity Measurements of Surfactant Foam in Porous Media -- SUPRI TR-48," U.S. Dept. of Energy Report DOE/SF/11564-13 (DE86000260) (December 1985).
11. Friedmann, F., and Jensen, J.A.: "Some Parameters Influencing the Formation and Propagation of Foams in Porous Media," SPE 15087, presented at the 1986 California Regional Meeting of SPE, Oakland, CA, April 2-4.

12. De Vries, A.S. and Wit, K.: "Rheology of Gas/Water Foam in the Quality Range Relevant to Steam Foam," SPE 18075, presented at the 1988 Annual Technical Conference and Exhibition of the SPE, Houston, TX, October 2-5.
13. Patzek, T.W.: "Description of Foam Flow in Porous Media by the Population Balance Method," Surfactant-Based Mobility Control, Smith, D.H., ed., ACS Symposium Series, Vol. 373, 326-341 (1988).
14. Parsons, R.W.: "Microwave Attenuation - A New Tool for Monitoring Saturations in Laboratory Flooding Experiments," SPEJ (August 1975) 302-310.
15. Sharma, D.K.: "Kinetics of Oil Bank Formation," Ph.D. Thesis, University of California, Berkeley (1987).
16. Ettinger, R.A.: "Flow Resistance of Foam in Berea Sandstone," M.S. Thesis, University of California, Berkeley, in preparation (1989).
17. Udell, K.S. and Radke, C.J.: "Mechanisms of Mobility Control with Foams," DOE Enhanced Oil Recovery Progress Review, (DE87001256) Vol. 50, 75-76 (March 1988).
18. Carl Zeiss, Inc.: "TGZ3 and TGZ3 Automatic Particle Size Counter: Operating Instructions," Oberkochen, West Germany.

19. Ransohoff, T.C. and Radke, C.J.: "Mechanisms of Foam Generation in Glass-Bead Packs," SPERE (May 1988) 573-585.
20. Wardlaw, N.C., Li, Y., and Forbes, D.: "Pore-Throat Size Correlation from Capillary Pressure Curves," Transport in Porous Media (December 1987) 597-614.
21. Manlowe, D.J.: "Pore-Level Mechanisms of Foam Destabilization by Oil in Porous Media," M.S. Thesis, University of California, Berkeley (1988).
22. Jimenez, A.I. and Radke, C.J.: "Dynamic Stability of Foam Lamellae Flowing Through a Periodically Constricted Pore," presented at the Symposium on Advances in Oil Field Chemistry, Third Chemical Congress of the North American Continent and 195th National Meeting of ACS, Toronto, Canada, June 5-11 (1988).
23. Bernard, G.G., Holm, L.W., and Jacobs, W.L.: "Effect of Foam on Trapped Gas Saturation and on Permeability of Porous Media to Water," SPEJ (December 1965) 295-300.
24. Holm, L.W.: "The Mechanism of Gas and Liquid Flow Through Porous Media in the Presence of Foam," SPEJ (December 1968) 359-369.
25. Nahid, B.H.: "Non-Darcy Flow of Gas Through Porous Media in the Presence of Surface Active Agents," Ph.D. Thesis, University of Southern California, Los Angeles (1971).

26. Huh, D.G. and Handy, L.L.: "Comparison of Steady- and Unsteady-State Flow of Gas and Foaming Solution in Porous Media," SPERE (February 1989) 77-84.
27. Gauglitz, P.A., St. Laurent, C.M., and Radke, C.J.: "An Experimental Investigation of Gas-Bubble Breakup in Constricted Square Capillaries," JPT (Sept. 1987) 1137-1146.
28. Ransohoff, T.C., Gauglitz, P.A., and Radke, C.J.: "Snap-Off of Gas Bubbles in Smoothly Constricted Noncircular Capillaries," AIChE Journal (May 1987) 753-765.
29. Chambers, K.T.: "Pore-Level Mechanisms and Modeling of Foam Flow in Porous Media," M.S. Thesis, University of California, Berkeley, in preparation (1989).
30. Shirley, A.I.: "Foam Formation in Porous Media, A Microscopic Visual Study," Surfactant-Based Mobility Control, Smith, D.H. ed., ACS Symposium Series, Vol. 373, 234-257 (1988).
31. Khatib, Z.I., Hirasaki, G.J., and Falls, A.H.: "Effects of Capillary Pressure on Coalescence and Phase Mobilities in Foams Flowing Through Porous Media," SPERE (August 1988) 919-926.

FIGURE CAPTIONS

- Figure 1. Schematic of foam-flow apparatus.
- Figure 2. Pressure profiles for strong foam (closed symbols, $U = 2.5$ m/day) and weak foam (open symbols, $U = 0.91$ m/day). Exit gas fractional flow is 0.90.
- Figure 3. Effluent foam texture: (a) weak foam ($D_{BL} \approx 700 \mu\text{m}$), (b) strong foam ($D_{BL} \approx 300 \mu\text{m}$).
- Figure 4. Pressure drop across the core per unit length versus velocity for pregenerated (closed symbols) and in-situ generated (open symbols) foam flow experiments.
- Figure 5. Liquid saturation profiles
- Figure 6. Injected and effluent bubble size distributions: $U = 0.91$ m/day and $f_g = 0.70$.
- Figure 7. Exit bubble-size distributions for pregenerated (solid line) and in-situ generated (dashed line) foam flow experiments: $U = 0.91$ m/day and $f_g = 0.70$.
- Figure 8. Exit average bubble densities and sizes versus velocity for pregenerated (closed symbols) and in-situ generated (open symbols) foam flow experiments.

Figure 9. Dimensionless bubble density profiles at $Da = 10$ and for various compressibility factors, κ . Dashed lines represent the local-equilibrium approximation.

Figure 10. Dimensionless pressure profiles at $Da = 10$ and for various compressibility factors, κ . Dashed lines represent the local-equilibrium approximation.

Figure 11. Bubble density profiles for pregenerated (closed symbols) and in-situ generated (open symbols) foam flow experiments: $U = 0.91$ m/day and $f_g = 0.70$. Model predictions (solid lines) and the local-equilibrium approximation (dashed lines) are shown. Fitting parameters are listed in Table 1.

Figure 12. Dimensionless pressure profiles for pregenerated (closed symbols) and in-situ generated (open symbols) foam flow experiments: $U = 0.91$ m/day and $f_g = 0.70$. Model predictions (solid lines) and the local-equilibrium approximation (dashed lines) are shown. Fitting parameters are listed in Table 1.

Table 1. Parameter Values.

Parameter	Value
m	1/3
n	1
k_1	$0.784 \text{ cm}^{-1/3} \text{ s}^{-2/3} \text{ mm}^{-3}$
k_{-1}	1 cm^{-1}
η	1.3

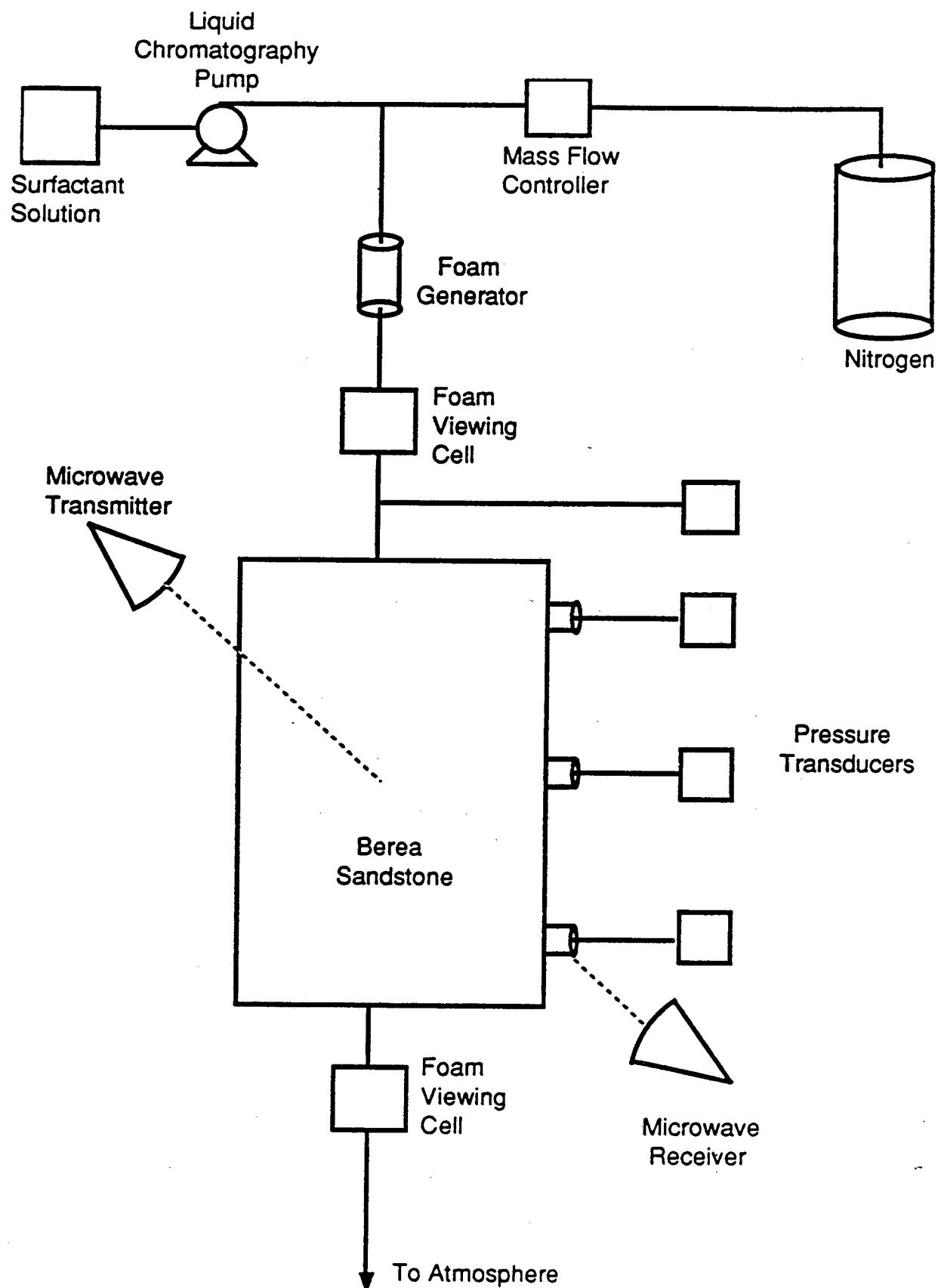


Figure 1 — Schematic of foam-flow apparatus

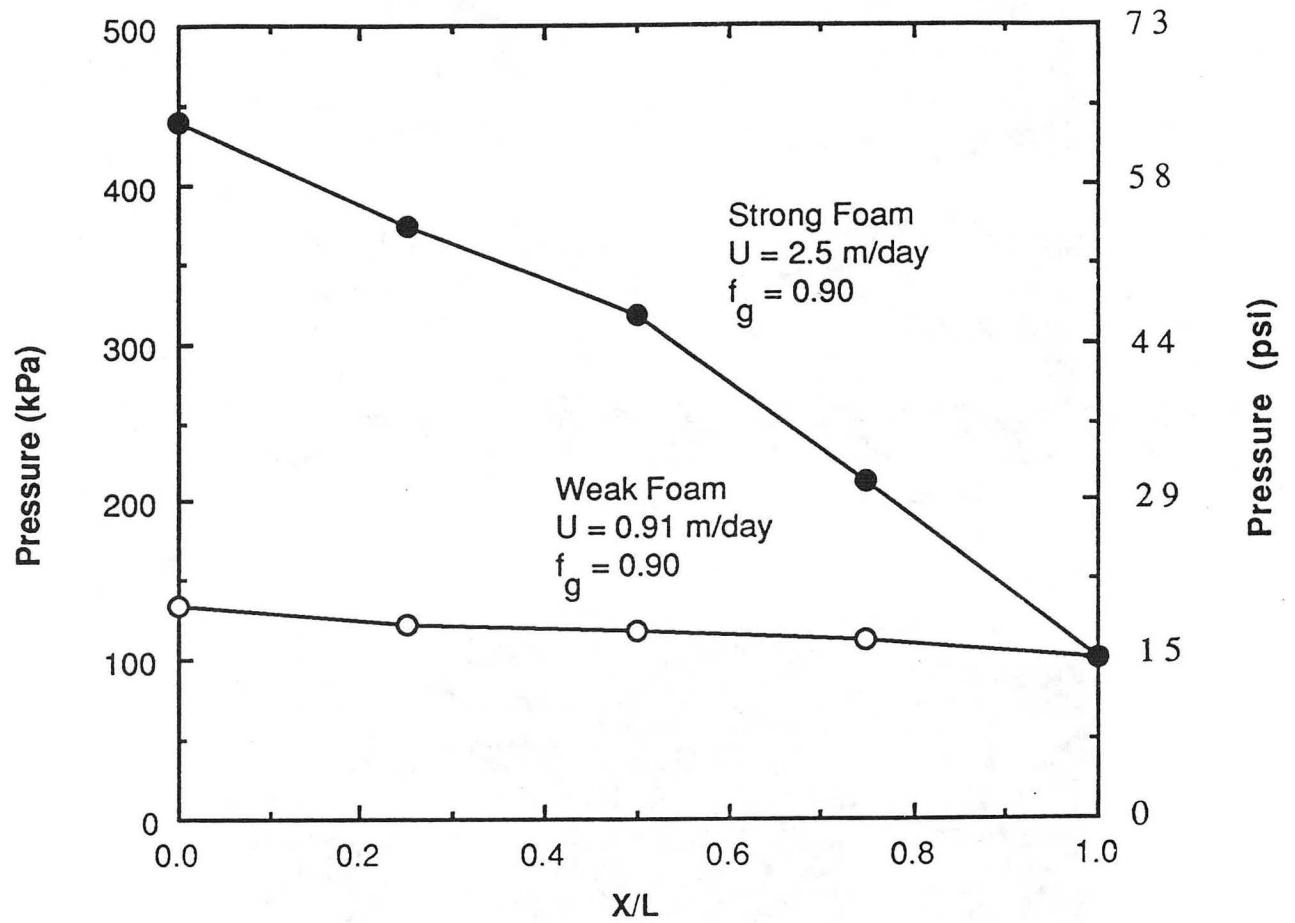
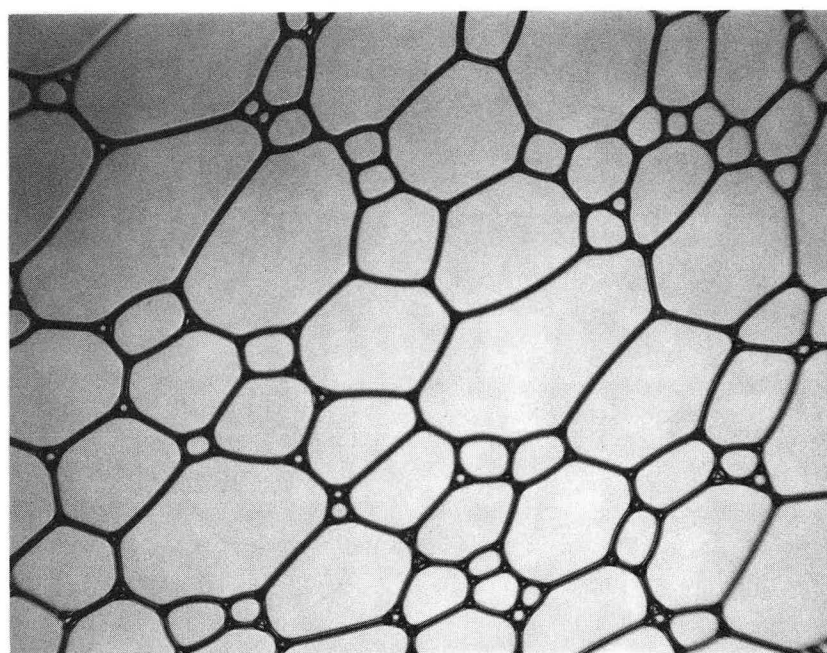
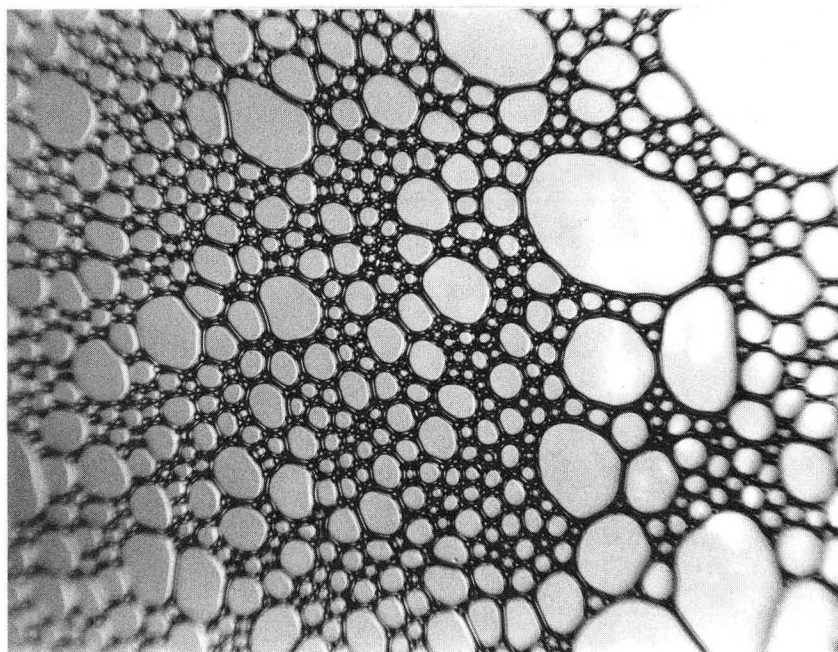


Figure 2 — Pressure profiles for strong foam (closed symbols, $U = 2.5$ m/day) and weak foam (open symbols, $U = 0.91$ m/day). Exit gas fractional flow is 0.90.



1 mm

(a)



1 mm

(b)

Figure 3 — Effluent foam texture: (a) weak foam ($D_{BL} \sim 700\mu\text{m}$),
(b) strong foam ($D_{BL} \sim 300\mu\text{m}$).

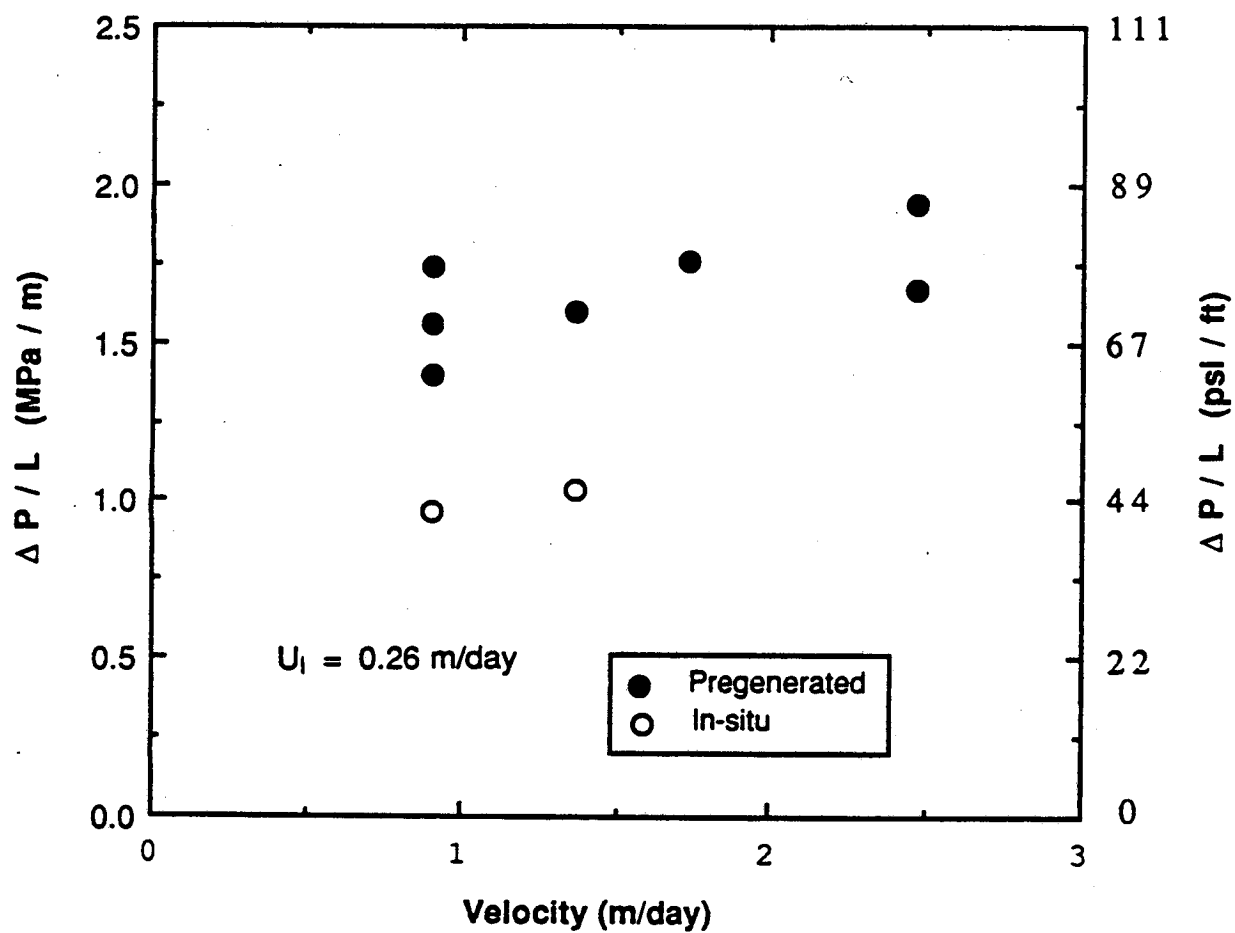


Figure 4 — Pressure drop across the core per unit length versus velocity for pregenerated (closed symbols) and in-situ generated (open symbols) foam flow experiments.

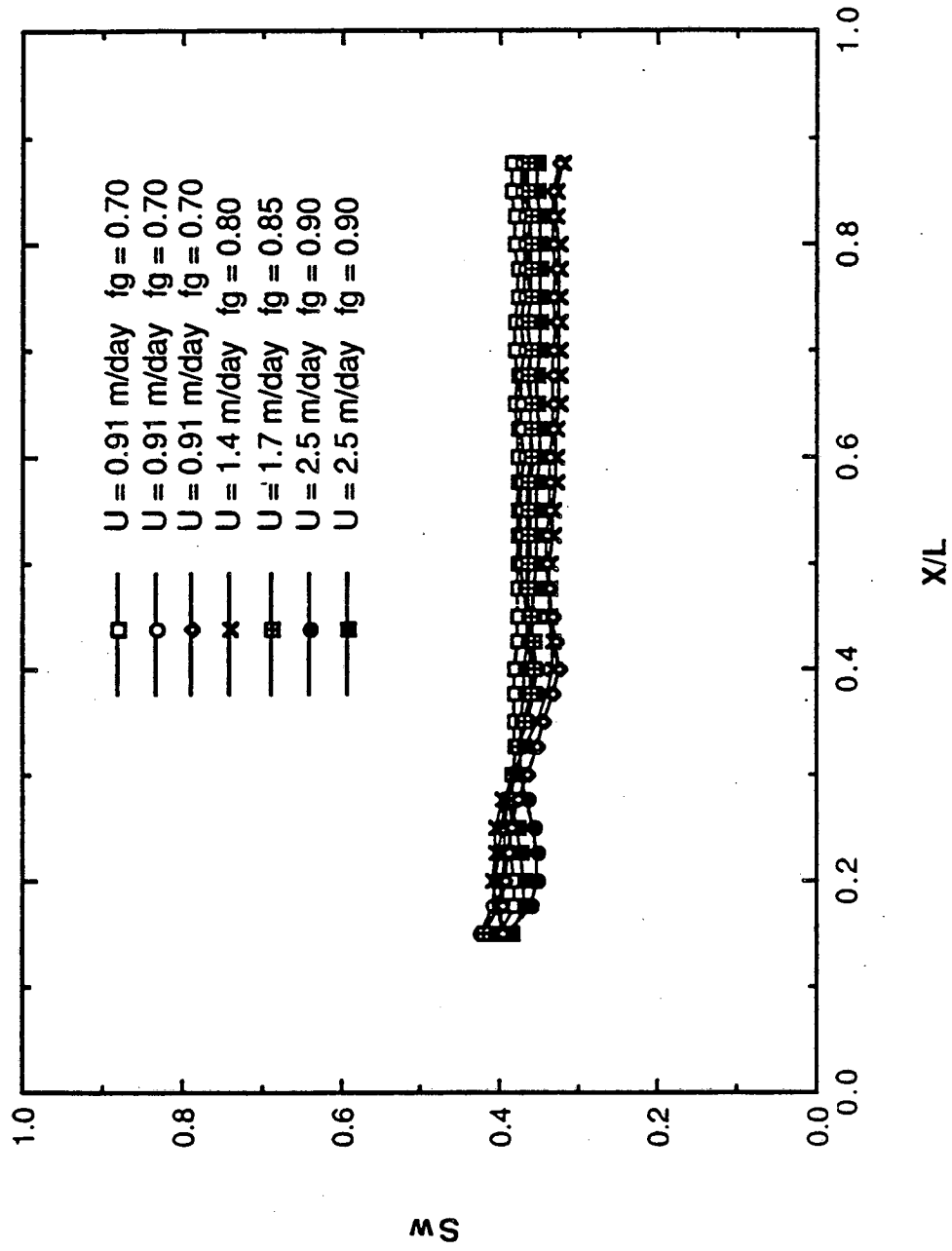


Figure 5 — Liquid saturation profiles.

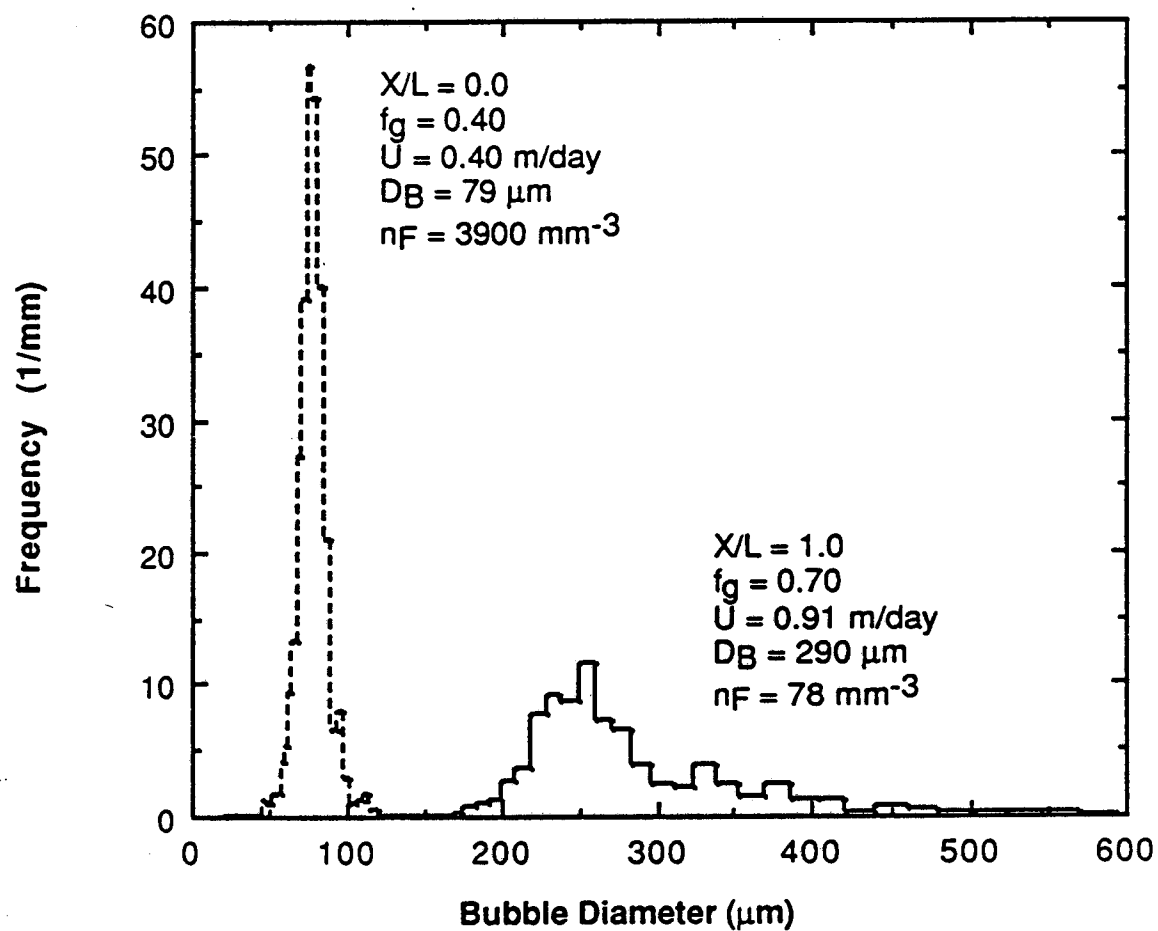


Figure 6 — Injected and effluent bubble size distributions: $U = 0.91 \text{ m/day}$ and $f_g = 0.70$.

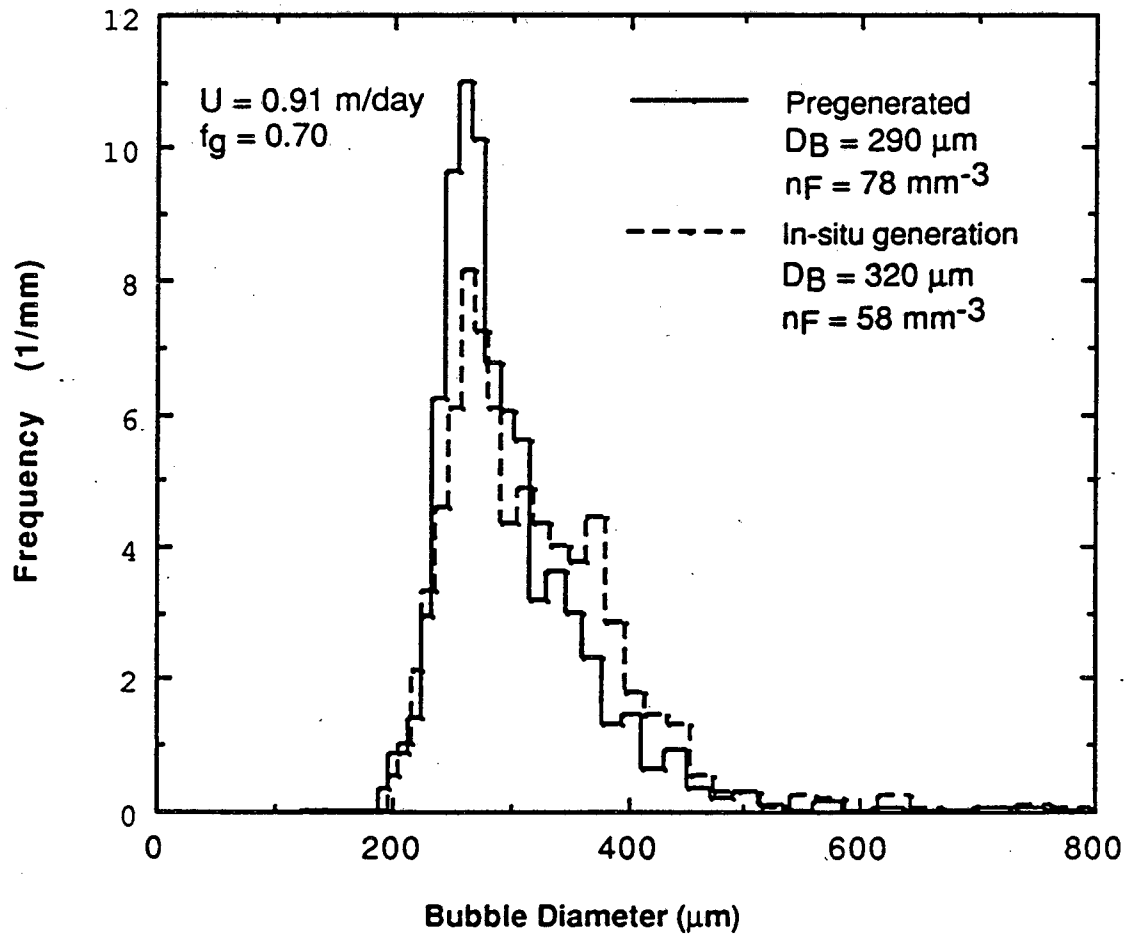


Figure 7 — Exit bubble-size distributions for pregenerated (solid line) and in-situ generated (dashed line) foam flow experiments: $U = 0.91 \text{ m/day}$ and $f_g = 0.70$.

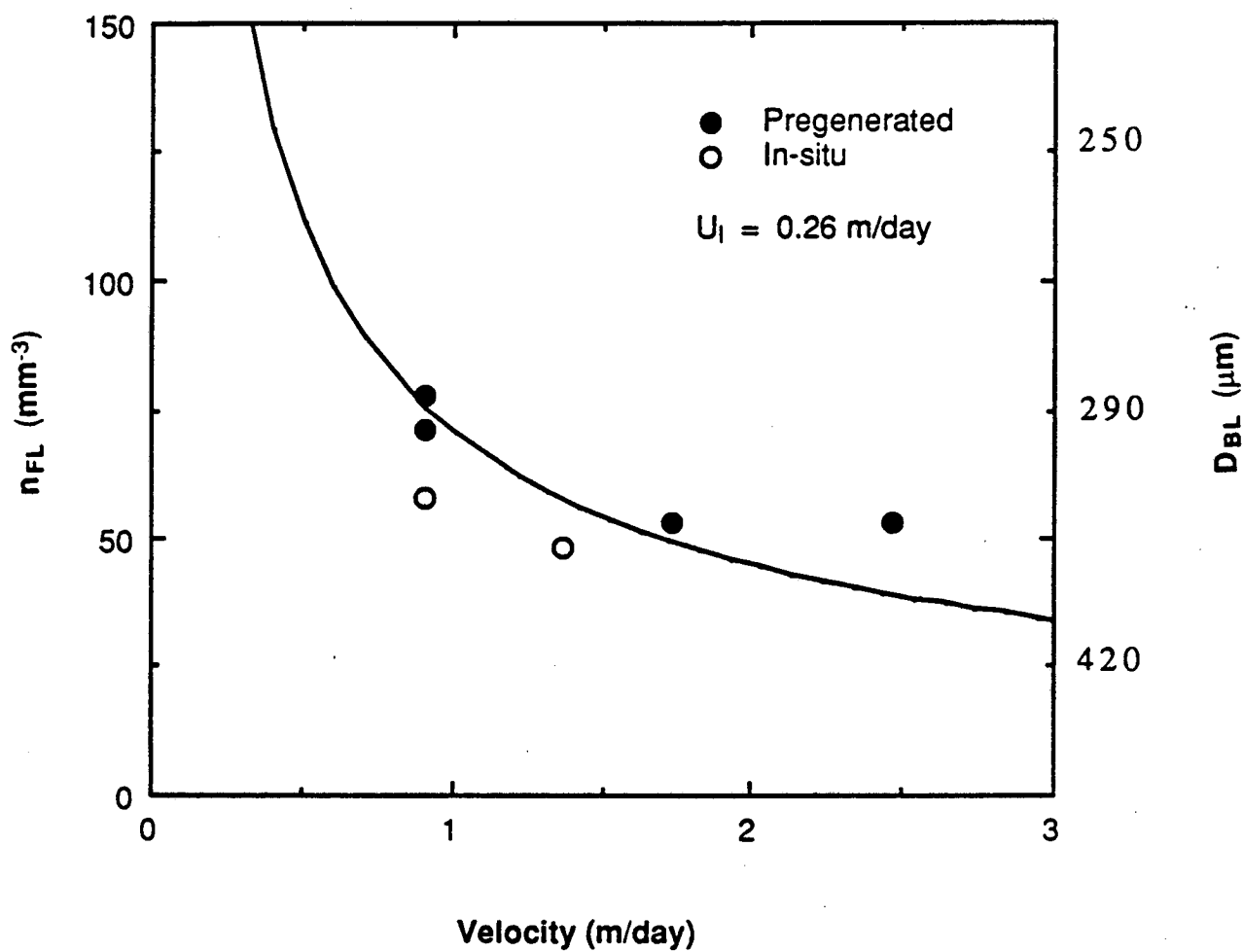


Figure 8 — Exit bubble densities and sizes versus velocity for pregenerated (closed symbols) and in-situ generated (open symbols) foam flow experiments.

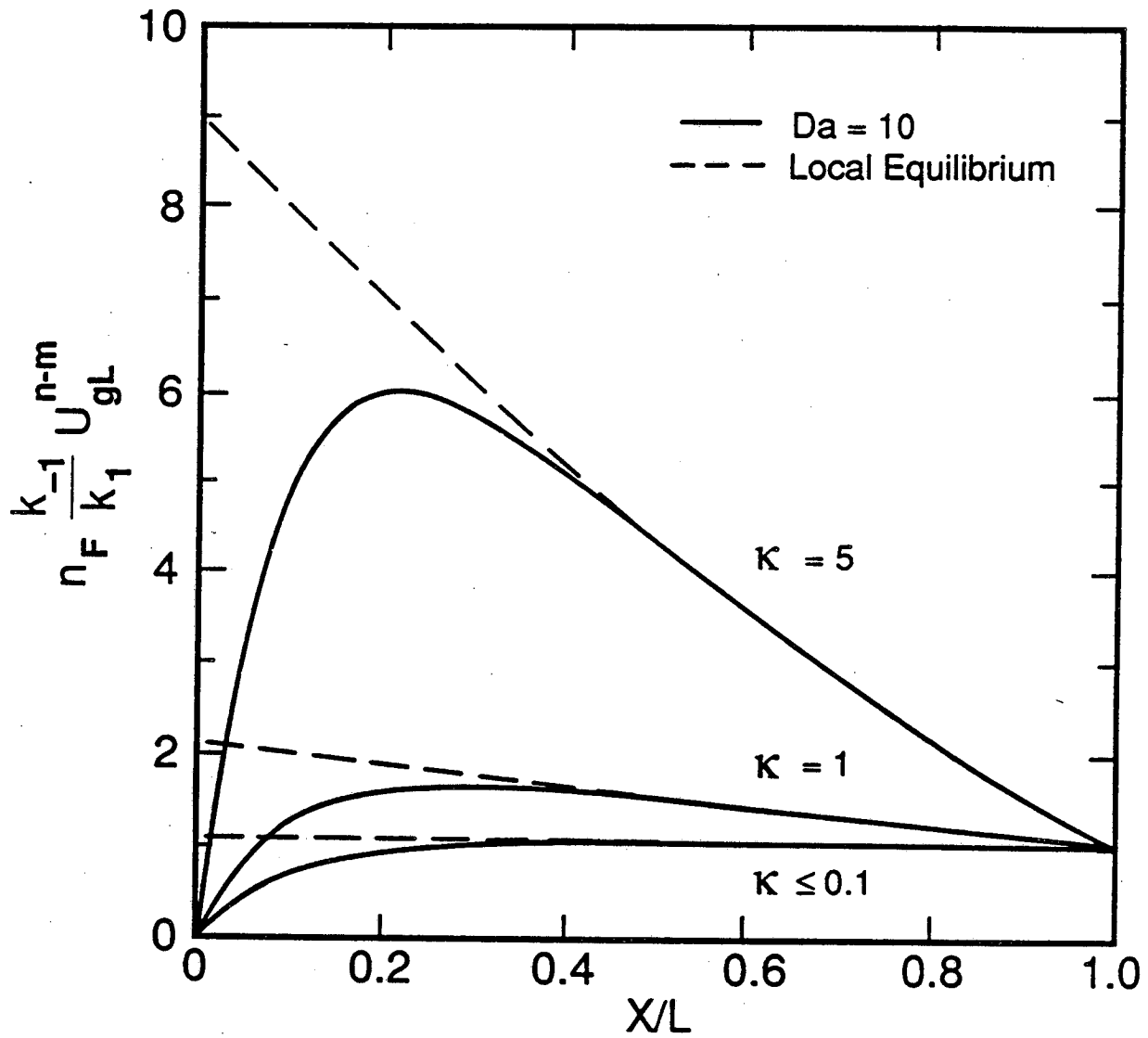


Figure 9 — Dimensionless bubble density profiles at $Da = 10$ and for various compressibility factors, κ . Dashed lines represent the local equilibrium approximation.

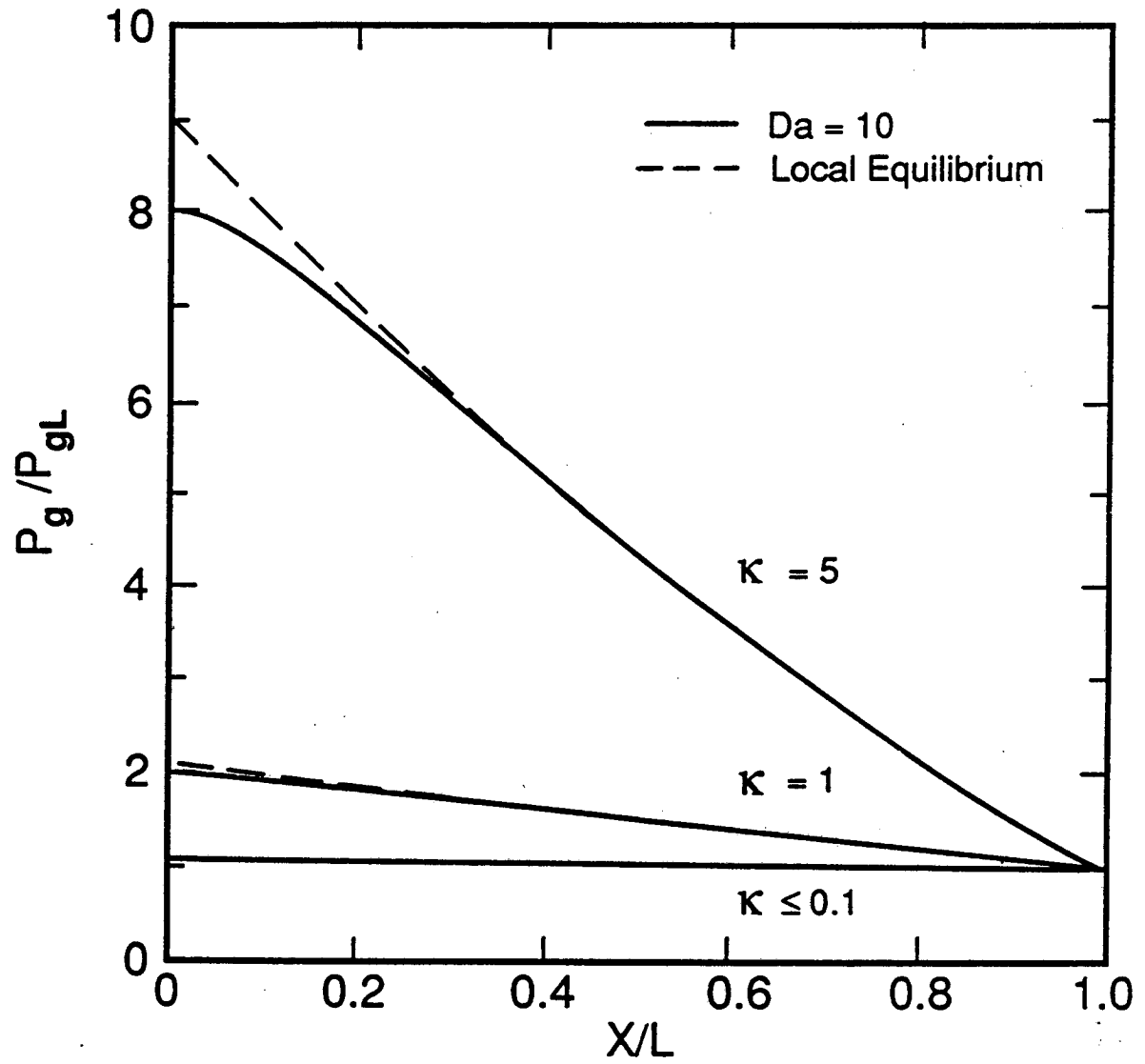


Figure 10 — Dimensionless pressure profiles at $Da = 10$ and for various compressibility factors, κ . Dashed lines represent the local-equilibrium approximation.

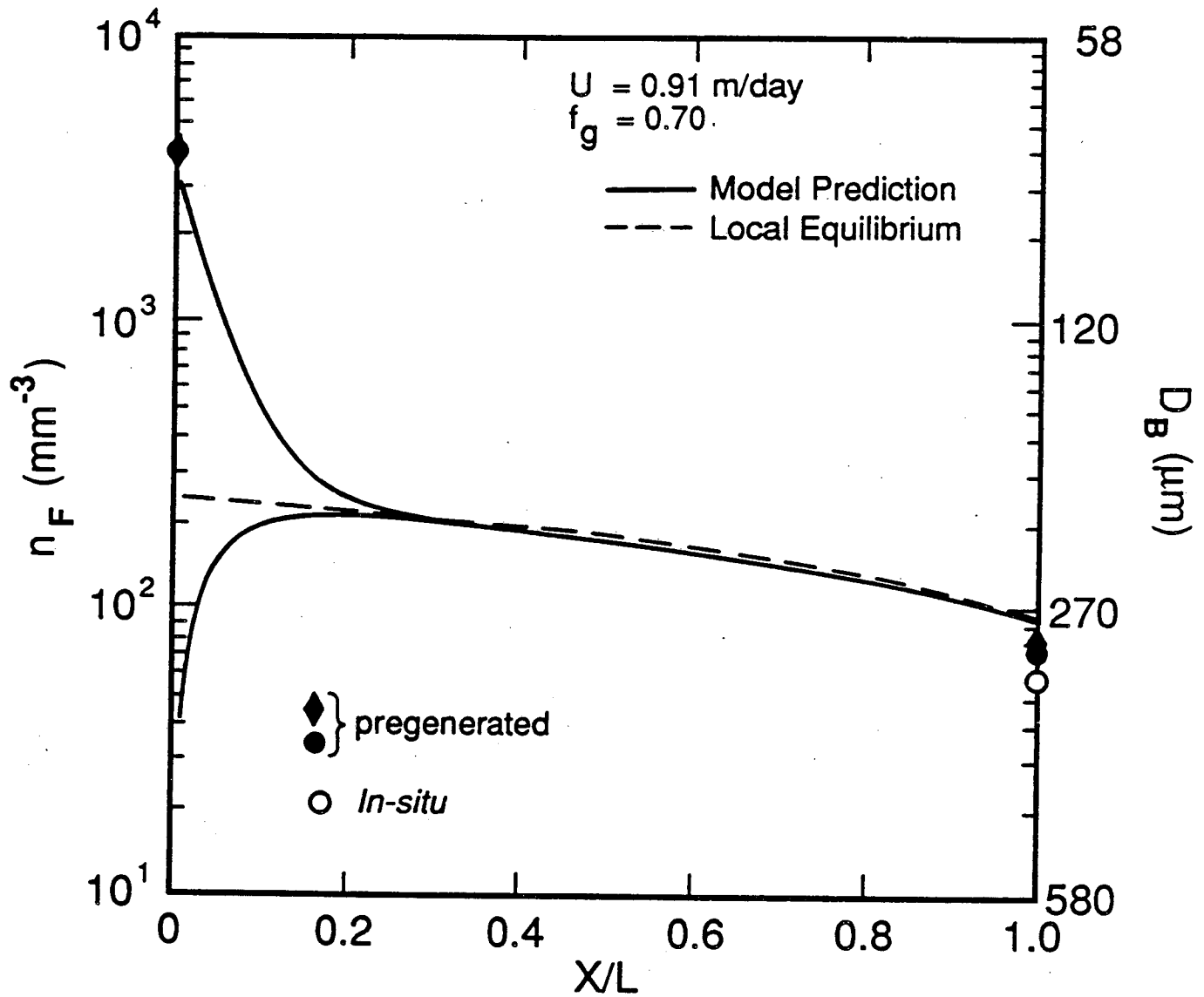


Figure 11 — Bubble density profiles for pregenerated (closed symbols) and in-situ generated (open symbols) foam flow experiments: $U = 0.91 \text{ m/day}$ and $f_g = 0.70$. Model predictions (solid lines) and the local-equilibrium approximation (dashed lines) are shown. Fitting parameters are listed in Table 1.

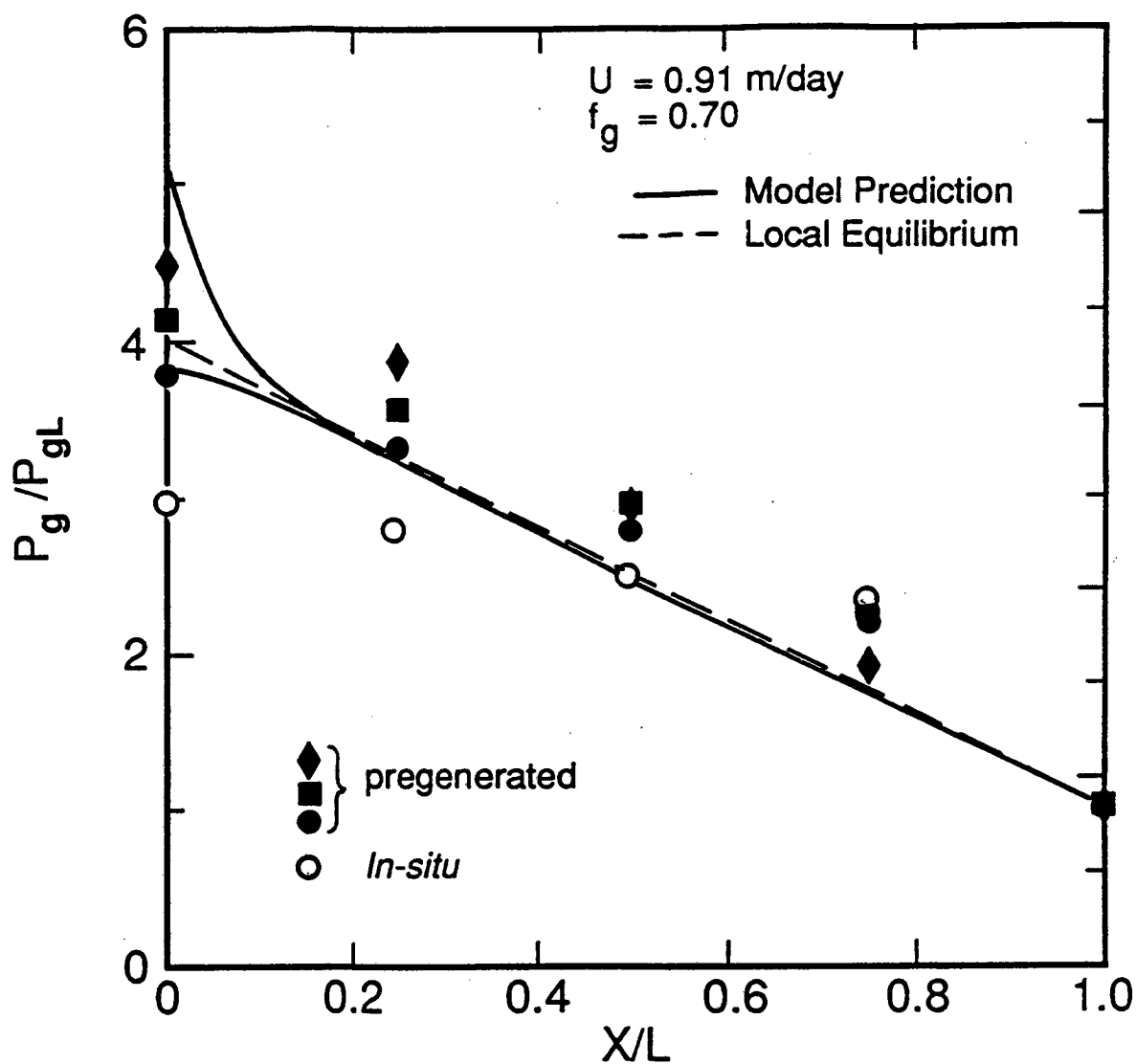


Figure 12 — Dimensionless pressure profiles for pregenerated (closed symbols) and in-situ generated (open symbols) foam flow experiments: $U = 0.91$ m/day and $f_g = 0.70$. Model predictions (solid lines) and the local-equilibrium approximation (dashed lines) are shown. Fitting parameters are listed in Table 1.

LAWRENCE BERKELEY LABORATORY
TECHNICAL INFORMATION DEPARTMENT
UNIVERSITY OF CALIFORNIA
BERKELEY, CALIFORNIA 94720